Scilight

Advanced Characterization

https://www.sciltp.com/journals/ac

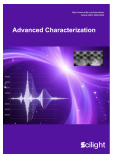

Review

Spectroscopic Advances towards the Fundamental Understanding of CeO_x Interfaces in Model Catalysis Reactions

Jinyang Xu [1,2], Wei Sun [1,2], Zhaofeng Liang [3], Hongbing Wang [1,2], Lei Xie [3], Bingbao Mei [3], Jingyuan Ma [3] and Fei Song [1,2,3,*]

[1] Shanghai Institute of Applied Physics, Chinese Academy of Sciences, Shanghai 201800, China
[2] University of Chinese Academy of Sciences, Beijing 100100, China
[3] Shanghai Advanced Research Institute, Chinese Academy of Sciences, Shanghai 201210, China
* Correspondence: songfei@sinap.ac.cn

How To Cite: Xu, J.; Sun, W.; Liang, Z.; et al. Spectroscopic Advances towards the Fundamental Understanding of CeO_x Interfaces in Model Catalysis Reactions. *Advanced Characterization* **2026**, *1*(1), 22–39.

Received: 20 March 2026
Revised: 23 April 2026
Accepted: 29 April 2026
Published: 20 May 2026

Abstract: Synchrotron-based X-ray spectroscopy has revolutionized the study of cerium oxide (CeO_x) model catalysts by providing unprecedented insight into their structure-activity relationships. Techniques such as X-ray absorption spectroscopy (XAS) and resonant photoelectron spectroscopy (RPES) have played pivotal roles in characterizing the concentration, electronic consequences, and reactivity of oxygen vacancies (O_vs), as well as the Ce^{3+}/Ce^{4+} redox couple, under *in situ* and operando conditions. Recent advances in Near-ambient-pressure X-ray photoelectron spectroscopy (NAP-XPS) have further enabled the direct observation of surface intermediates and dynamic changes in cerium oxidation state during catalytic reactions, thereby moving beyond the limitations of idealized ultra-high-vacuum studies. Looking forward, the next frontier lies in exploiting the high spatial resolution of nano-focused X-ray beams and the ultrafast time resolution of X-ray free-electron lasers (XFELs) to identify active sites and capture transient species throughout catalytic cycles. These advanced synchrotron techniques are expected to play an essential role in guiding the rational design of next-generation CeO_x-based catalysts for energy and environmental applications.

Keywords: NAP-XPS; XAS; CeO_x interfaces; synchrotron-based spectroscopy

1. Introduction

Cerium oxides are widely studied as reducible oxides in heterogeneous catalysis because their roles go beyond just acting as passive supports [1,2]. The reversible Ce^{4+}/Ce^{3+} redox pair, significant oxygen storage-release capacity (OSC), and the relative ease of O_vs formation and refill make CeO_x particularly responsive to the reaction environment and important in processes such as oxidation, reforming, water-gas shift, CO_2 conversion, and other energy-related catalysis [2,3]. However, these characteristics also make mechanistic analysis challenging, since the active state often exists under operating conditions and can differ greatly from that observed in ex situ characterization [4]. Therefore, a key challenge in CeO_x catalysis is not only identifying morphologies but also understanding how O_vs, Ce oxidation valence states, and interfacial electronic structures evolve during reactions and how these changes affect catalytic performance [1,4].

This issue is especially crucial at CeO_x interfaces, where catalytic performance often depends on the interaction of surface structure, defect chemistry, and metal-oxide interactions [1,5]. Surface science studies demonstrate that CeO_x reactivity heavily relies on crystallographic orientation and surface coordination environment, and that reconstruction can alter the terminations present under relevant conditions [2,5]. Therefore, ceria nanorods cannot be understood solely through idealized facet assignments. Extensive faceting and

reconstruction may expose a significant portion of {111} nanofacets, making particle morphology alone an inadequate descriptor of the active surface [5]. At metal-ceria interfaces, the situation becomes more complex due to charge redistribution across the boundary. In Pt/CeO_2 model systems, synchrotron-based studies reveal that interfacial electron transfer depends on particle size and can be directly measured, establishing metal-support charge exchange as a quantifiable mechanistic parameter rather than just a qualitative concept [6]. Similarly, atomically dispersed Pt^{2+} species on nanostructured CeO_2, according to combined photoelectron spectroscopy, resonant photoemission, and density functional theory (DFT) calculations, are not intrinsically active for H_2 dissociation; instead, hydrogen activation involves trace metallic Pt and is coupled with Ce^{4+} reduction, reverse oxygen spillover, and the formation of O_vs [7]. Reduced CeO_{2-x} thin films exhibit vacancy-mediated redox chemistry that redirects the breakdown of adsorbed oxygenates by shifting the balance between C–C and C–O bond cleavage [8]. Collectively, these studies clearly demonstrate that a static description of CeO_x is inadequate, and the active state of the oxide and its interface must be understood under reaction conditions [5–8].

Synchrotron-based X-ray spectroscopy has become indispensable in this context because each method resolves a different part of the working CeO_x interface [4,9,10]. NAP-XPS is the most direct approach for following surface and near-surface chemistry, including Ce^{3+}/Ce^{4+} ratios, oxygen-vacancy-related oxygen components, and adsorbate-derived intermediates in reactive atmospheres [4]. Recent NAP-XPS work on CeO_x foil further showed that the surface Ce^{3+} population can be reversibly tuned under UHV, O_2, H_2, and CO_2, while vacancy-rich Ce^{3+} sites recover after CO_2 removal, underscoring that even the redox descriptors of ceria itself are working-state quantities rather than fixed material constants [11]. RPES offers complementary sensitivity to Ce^{3+}/Ce^{4+} species and interfacial electronic structure, which has proved particularly valuable in well-defined metal/CeO_x model catalysts [6,7]. Fluorescence-detected XAS, including high-energy-resolution fluorescence-detected measurements, addresses a different limitation: although it is less surface-selective than photoemission, it can probe dilute species, buried interfaces, and catalysts under more realistic gas, temperature, or electrochemical environments [9,12,13].

These methods are therefore complementary rather than interchangeable. NAP-XPS is strongest for assigning surface oxidation states and adsorbates, but its use is constrained by the shallow escape depth of photoelectrons, the pressure window, charging on poorly conducting oxides, and the difficulty of accessing solid-liquid interfaces directly [4,12,13]. By contrast, XAS and high-energy-resolution XAS average over a larger information depth and usually require complementary probes to identify surface-specific intermediates, but they remain powerful for operando studies of low-loading catalysts and buried interfaces [9,10,12,13]. Recent instrumental developments have strengthened this combined approach by integrating wide-energy-range XPS, Hard X-ray Photoelectron Spectroscopy (HAXPES), Total Electron Yield X-ray Absorption Spectroscopy (TEY-XAS), extended X-ray absorption fine structure (EXAFS), and High-Energy-Resolution Fluorescence-Detected X-ray Absorption Spectroscopy (HERFD-XAS) on dedicated *in situ* platforms, making it increasingly practical to correlate surface chemistry with element-specific local structure within a common experimental framework [12–14].

The relevance of this spectroscopic perspective extends across thermal catalysis, photocatalysis, and electrocatalysis, but the nature of active-state formation differs substantially among these fields. In thermal catalysis, CeO_2-supported systems are key to reactions like reverse water-gas shift, where O_vs, metal-support interaction, and facet-dependent stabilization of intermediates greatly influence activity and selectivity [15]. In photocatalysis, CeO_x-based composites continue to draw interest because their 4f electronic structure, defect chemistry, and heterojunction design enable tuning light absorption, charge separation, and small molecule activation, although wide band gaps and carrier recombination still present challenges [3,16]. In electrocatalysis, Ce-based materials and CeO_x-containing interfaces are being studied for oxygen evolution and reduction reactions because their redox flexibility and O_vs chemistry boost oxygen adsorption, interfacial charge transfer, and catalytic turnover, despite the low intrinsic conductivity of pristine ceria being a major limitation [17]. Across these fields, the central challenge is to determine how CeO_x interfaces evolve into catalytically relevant states under working conditions. This problem cannot be resolved from the precatalyst structure alone, because the oxidation state, local coordination, vacancy-related structure, and adsorbate population of CeO_x often change substantially during operation conditions [4,9,10]. In this respect, synchrotron-based spectroscopy has provided a decisive advantage by enabling these changes to be followed directly [4,9]. From this perspective, the following discussion considers recent spectroscopic advances in model systems, with particular emphasis on how XAS, RPES, and NAP-XPS have been used to identify the structure, dynamics, and reactivity of CeO_x interfaces across the three major catalytic regimes addressed in this review. Before turning to the individual case studies, it is useful to state the comparative framework more explicitly. In thermal catalysis, active-state formation is driven mainly by gas composition and temperature [4,15]. In photocatalysis, illumination adds an additional driving force by perturbing carrier populations and interfacial charge separation [3,16]. In electrocatalysis, the working interface is created under

applied bias and in contact with electrolyte, so potential, local pH, ion adsorption, and mass transport become part of the structure-forming environment [14,17]. Accordingly, the most informative operando observables and the main characterization challenges are not identical across these three fields. To facilitate cross-field comparison, representative working-state CeO_x interfacial motifs, key operando/*in situ* observables, associated elementary steps, and catalytic functions across thermal catalysis, photocatalysis, and electrocatalysis are summarized in Table 1.

Table 1. Comparison of representative working-state CeO_x interfacial motifs, operando/*in situ* observables, associated elementary steps, and catalytic functions across thermal catalysis, photocatalysis, and electrocatalysis.

Regime	Interface	Technique	Main Observable	Intermediate	Catalytic Function
Thermal catalysis [18–23]	Ni/CeO_x	NAP-XPS, XAS, DRIFTS	Ni L_3-edge/Ce M_5-edge; Ni^0/Ni^{2+}; Ce^{3+}/Ce^{4+} ratio	CO_2 activation; carbonate/formate hydrogenation	Stabilizes mixed interfacial states for methanation
Thermal catalysis [24–29]	Cu/CeO_x	XRD, XAS, NAP-XPS, UV-Raman	Cu oxidation state; Ce^{3+} population; carbonate/formate coverage	H_2O dissociation; CO_2 activation; formate/carbonate	Promotes vacancy-mediated H_2O/CO_2 activation
Thermal catalysis [30–35]	$Pt^0–O_v–Ce^{3+}$; Pt/CeO_x	NAP-XPS, XAS, DRIFTS	Pt/Ce valence-state changes	H_2O dissociation; low-temperature CO oxidation	Creates stabilized reaction-induced active sites
Photocatalysis [36]	$Pt/CeO_2/TiO_2$	XAS, DRIFTS	Ce/Pt state evolution	CH_3OH activation; decarbonylation; WGS reaction;	Couples charge transfer with surface redox
Photocatalysis [37,38]	$Ni–O_v–Ce^{3+}$	DRIFTS, Raman, XAS, UV-vis	Vacancy-rich Ni–CeO_x sites	CH_4 activation; CO_2 activation	Forms the active Ni–CeO_x interface under light
Photocatalysis [39]	$Ce^{4+}–O–Ce^{4+} \rightleftharpoons Ce^{3+}–O_v–Ce^{3+}$	XPS, EPR, DRIFTS	Ce^{3+} concentration; transient CO formation	Vacancy-mediated CO_2 to CO redox cycle	CeO_x acts as a redox interface
Electrocatalysis [40–44]	CeO_2/Cu	XAS, Raman, vibrational spectroscopy	Cu K-edge; Ce L_3-edge	*CHO formation; C–C coupling/CH_4 formation	Controls CO_2RR selectivity; Stabilizes working states
Electrocatalysis [45–48]	CoO_x/CeO_x	Raman, XAS	Co K-edge; Ce L_3-edge	OER intermediate stabilization at Co-centered sites	Modulates Co redox behavior

2. Thermal Catalysis

2.1. Structure Sensitivity of CeO_x Interfaces

Thermal catalysis has provided clear evidence that the chemistry of CeO_x interfaces is highly sensitive to structure under working conditions. Nanoscale studies show that the exposed termination, vacancy formation energy, oxygen mobility, and metal-support interaction all change with crystal shape and particle size, and these factors are often interconnected rather than independent [49]. This was especially clear when rod-like ceria nanoparticles, often discussed as if they exposed only high-energy {110}/{100} facets, were observed to undergo faceting and reconstruction, revealing a significant amount of {111} nanofacets instead [5]. The key takeaway for catalysis is straightforward that labels based on morphology alone are unreliable indicators of the active CeO_x surface. Even during oxidation reactions, the ceria crystal plane influences which metal state is stabilized at the interface. For Pd/CeO_2, rods with more reducible terminations favor Pd–O–Ce environments and low-temperature CO oxidation, while octahedra dominated by {111} facets better preserve PdO species and perform better in propane oxidation [50].

2.2. Ni/CeO_2 Interfacial Structures in CO_2 Methanation

This sensitivity to the exact interfacial motif is most clearly observed in Ni/CeO_2 methanation catalysts. In plasma-prepared Ni/CeO_2, the combination of time-resolved X-ray diffraction (XRD), XAS, ambient-pressure X-ray photoelectron spectroscopy (AP-XPS), and diffuse reflectance infrared Fourier transform spectroscopy (DRIFTS) revealed that high low-temperature activity is linked to small Ni particles strongly interacting with ceria through interfacial oxygen, rather than with metallic Ni alone [51]. A similar conclusion was reached when Ni nanoparticles were encapsulated in mesoporous ceria, that the increased activity correlated with greater access to Ni–CeO_2 contact and vacancy-rich boundary sites, which promote CO_2 activation and subsequent hydrogenation [52]. Chemical promotion shifts the interface similarly. Y doping reduces ceria particle size, enhances vacancy concentration, and boosts metal-support interaction in Ni/CeO_2, while Eu^{3+} doping also strengthens Ni–CeO_2 contact and improves low-temperature methanation [53,54]. More recently, direct defect engineering of the support has further clarified this relationship. Plasma-treated CeO_2 supports produce a highly defective interfacial CeO_x layer after Ni deposition, thereby enhancing Ni–CeO_x interaction and shifting the carbonate population toward bridged species that are more readily consumed during methanation [55].

Meanwhile, the Ni/CeO_2 literature does not support a universal relationship between catalytic performance and either vacancy density or Ni particle size. Reported size effects remain inconsistent: 8 nm Ni was identified as optimal in one study [56], while another found that the intrinsic rate decreased with increasing Ni size and that the smallest particles favored CO formation and transient carbon-induced deactivation [57]. A third study showed that the turnover frequency became nearly size-independent after normalization to the number of exposed Ni atoms, although the smallest particles remained less selective for CH_4 [58]. Chen et al. further argued that catalytic behavior is influenced less by particle size itself than by the amount of accessible Ni available for hydrogenation of formate-derived intermediates [59]. Overall, these results suggest a balance among exposed metallic Ni, interfacial Ni–CeO_x sites, and the local redox state of ceria, rather than a single geometric optimum.

Operando spectroscopy has been crucial for clarifying this balance precisely because ex situ characterization tends to overemphasize the pretreated metallic state [18,19]. *In situ* NAP-XPS during CO_2 methanation showed that the catalyst surface under steady reaction is not fully reduced, but instead contains Ni^0 together with a persistent oxidized Ni fraction and a dynamically changing Ce^{4+}/Ce^{3+} ratio [18]. This already indicates that the active interface cannot be described as metallic Ni particles on a static ceria support [18]. Soft X-ray absorption spectroscopy then strengthened this conclusion by following the Ni L_3-edge and Ce M_5-edge line shapes during activation and methanation light-off, where the evolution of ionic and metallic Ni occurs together with the reduction of ceria [19]. In that sense, the contribution of the two methods is complementary: NAP-XPS establishes the surface oxidation-state distribution under reaction gas, whereas operando soft XAS shows that the Ni–CeO_x motif evolves continuously as the catalyst enters the active temperature window [18,19]. Together, these measurements show that ionic Ni is not merely a precursor observed before reduction, but part of the working interfacial ensemble under methanation conditions [18,19]. As shown in Figure 1, the Ni L_3-edge evolves from a predominantly ionic signature after activation to a mixed ionic/metallic line shape as the catalyst passes through methanation light-off, while Figure 1b shows the concurrent increase in reduced ceria features at the Ce M_5 edge [19]. Figure 1c,d then connect these spectral changes to the onset of CO_2 conversion and CH_4 selectivity, showing that the most active state is reached only after the catalyst is already under reactive gas and elevated temperature [19]. This is precisely the kind of information that conventional ex situ characterization cannot provide: measurements before or after reaction would miss the transient coexistence of Ni^{2+}, Ni^0, and reduced ceria that defines the working Ni–CeO_x interface. The same group later showed that thermal treatment continuously redistributes this balance: calcination at 600 °C partially exsolves Ni and enhances methanation, whereas aging at 750 °C produces larger Ni particles, more CO, and surface carbon deposition [20]. XAS studies of Ni/CeO_2 prepared by the polymeric precursor route reached a related conclusion by linking high methane selectivity to catalysts in which Ni^0 is retained along with strong Ni–O–Ce interactions [21]. Similar behavior was reported for ceria-supported Ni examined by XAS, where sustained activity was associated with Ni reduction under reaction conditions and with a reduced ceria environment rather than with complete decoupling of metal and support [22]. A recent operando Raman study reveals that sonochemical synthesis produces a more defective ceria surface. These highly defective samples predominantly favor the formate-mediated pathway to CH_4, while less defective samples tend to produce CO [23].

2.3. Metal-Dependent Methanation Pathways on Rh–, Ru–, and Co/CeO_2

Rh–, Ru–, and Co–based catalysts demonstrate that the same CeO_2 support can yield markedly different chemistries, depending on the metal and its stabilization. Early *in situ* studies comparing Rh/CeO_2 and Ni/CeO_2 during atmospheric-pressure methanation directly observed Ce^{3+} formation, which was linked to CO_2 activation. The stronger interaction between Rh and ceria produced smaller particles and higher methane selectivity [60]. For Ru/CeO_2, Wang et al. suggested a vacancy-assisted formate route in which the O_vs is not merely a spectator but part of the active site; the conversion of formate-derived species then becomes kinetically critical [61]. However, Ru/CeO_2 does not follow a single universal mechanism. When single Ru atoms, nanoclusters, and nanoparticles were compared on ceria nanowires, the nanocluster sample was the most active, and *in situ* DRIFTS supported a dominant CO route where Ce^{3+}–OH sites assist CO_2 dissociation while Ru sites near the interface hydrogenate carbonyl species [62]. Support modification again shifts this balance. Doping Ru/CeO_2 with Cr^{3+} increases the surface concentration of both O_vs and hydroxyl groups. *In situ* FTIR combined with H_2-TPSR showed that both the CO and formate pathways are still present, but the formate route is much more promoted at low temperature [63]. Recent *in situ* XAFS and DRIFTS studies further showed that very small bidimensional Ru clusters and ultrathin nanoplates behave differently under CO_2/H_2 feeds: clusters are more easily reoxidized and generate more mixed CO/CH_4 behavior, whereas larger nanoplates can maintain high methane selectivity even though they are only a few atomic layers thick [64].

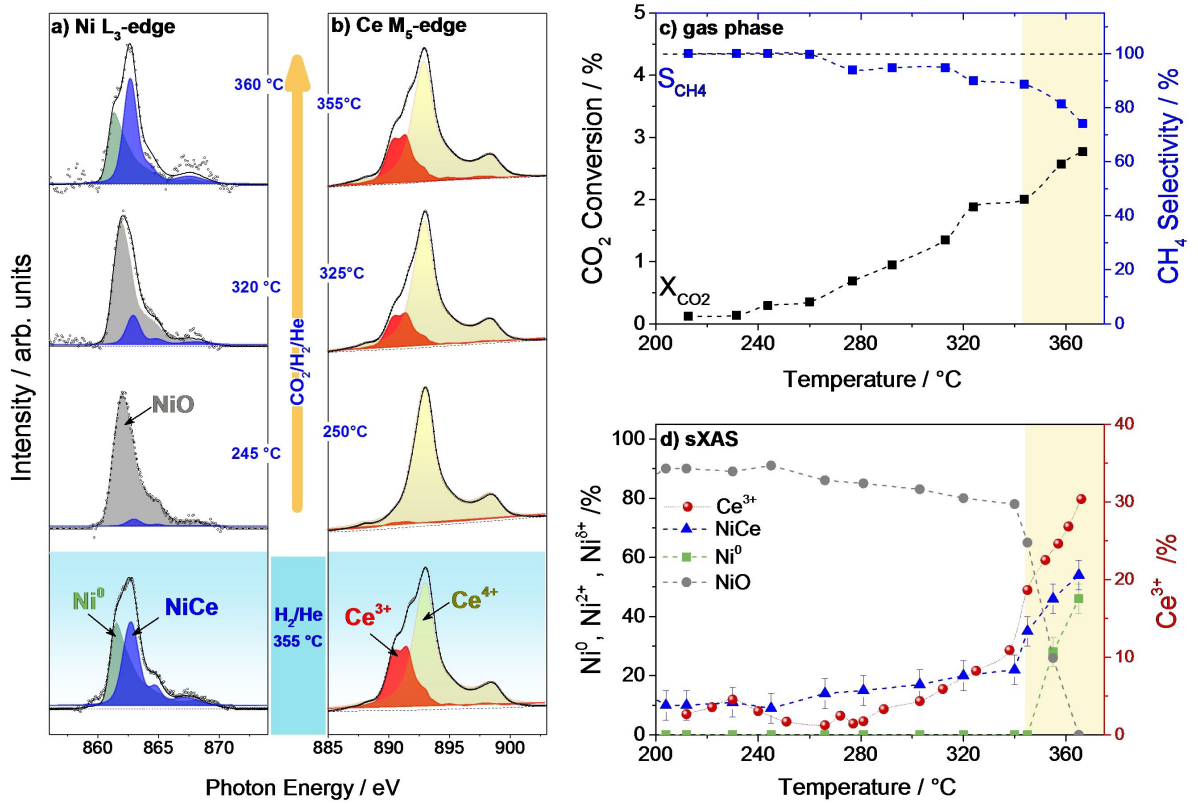

Figure 1. Operando soft X-ray absorption evidence for the working-state evolution of ionic and metallic Ni species in ceria-supported Ni catalysts during CO_2 methanation. (**a**) Ni L_3-edge and (**b**) Ce M_5-edge sXAS spectra of $NiCeO_x$ catalyst under activation and light-off CO_2 methanation reaction; (**c**) CO_2 conversion (XCO_2) and CH_4 selectivity (SCH_4) as a function of temperature measured in the sXAS cell by on-line GC; (**d**) evolution of various nickel and ceria oxidation states in the course of CO_2 methanation reaction obtained by the analysis of Ni L_3 and Ce M_5-edges respectively. Reproduced with permission [19]. Copyright 2023, Wiley-VCH.

The mechanistic understanding of Rh/CeO_2 has also become clearer. Modulation excitation spectroscopy on Rh/CeO_2 identified responsive carbonyl and carbonate species during H_2 pulsing, but formate was found to be either a spectator or part of a slow side reaction, making the main pathway less straightforward than often assumed [65]. More recently, the idea of a valence-restrictive metal-support interaction was introduced to explain why small Rh clusters on CeO_2 can be unusually active for methanation: the support limits Rh to a partially oxidized state that stabilizes negatively charged intermediates and active hydride species, thus favoring HCOO* chemistry and CH_4 formation, while isolated Rh sites favor COOH* and CO production [66]. Co/CeO_2 systems show the same dependence on the specific interface but are especially affected by loading levels. *In situ* X-ray absorption near-edge structure (XANES), EXAFS, NAP-XPS, and DRIFTS studies showed that low-loaded Co/CeO_2 contains more strongly perturbed Co species at the interface and exhibits weaker H_2 activation compared to higher-loaded catalysts, which generate more reducible and metallic cobalt [67]. Flame-synthesized $Co–CeO_2$ catalysts lead to the same conclusion via a different preparation method: low Co loading enhances Co^{2+}–O–Ce motifs and produces more CO, while larger metallic Co nanoparticles promote CH_4 formation [68]. Inverse CeO_x/Co catalysts further support this idea by showing that defective CeO_{2-x} clusters on Co nanoparticles can stabilize the metallic phase and enhance methanation performance [69]. On model $CoO_x/CeO_{2-\delta}\{100\}$ surfaces, *in situ* XAFS, XRD, DRIFTS, and environmental transmission electron microscopy (TEM) revealed that the interface itself is dynamic, undergoing size-dependent flattening, oxidation, and re-reduction when the gas phase switches to CO_2/H_2 [70].

2.4. Cu–CeO_x Interfaces in WGS, RWGS, and Methanol Synthesis

Cu/CeO_x catalysts are particularly valuable because they demonstrate how the same support can enable quite different reaction pathways. In the traditional $Cu–CeO_2$ water-gas shift system, time-resolved XRD, XAS, and DRIFTS revealed that turnover involves a cooperative site consisting of metallic Cu and ceria O_vs, where water dissociation occurs at vacancies or Cu-vacancy interfaces [24]. Morphology plays a role at the support level as well. For CuO/CeO_2 in WGS, nanospheres exhibited both higher activity and better stability than nanorods or nanocubes because the ceria shape influenced Cu dispersion, the stability of metallic Cu, and the ease of water

activation [25]. Under CO_2 hydrogenation conditions, hollow Cu/CeO_2 nanospheres showed a different but related outcome: *in situ* UV-Raman and DRIFTS indicated that bidentate carbonate and formate species form on vacancy sites, and the RWGS rate depends on the concentration of surface O_vs rather than Cu particle size [26]. However, this vacancy-centered perspective is not universal. On low-loaded $Cu/CeO_2(111)$, operando Raman, UV–vis, and transient IR suggested that a dominant redox mechanism, rather than an associative one, governs the process [27]. NAP-XPS on Cu/CeO_{2-x} similarly showed that the oxidation states of Cu and Ce change together with carbonate and formate coverages under reaction conditions, confirming that the working interface reconstructs in the reactive gas mixture. As shown in Figure 2, the combined spectra summarize the evolution of surface carbonate/formate species alongside the changes in Cu and Ce oxidation states, highlighting that the Cu–CeO_x interface is dynamically rebuilt under reactive atmospheres rather than remaining static in a metallic state [28]. On Fe-modified single-atom Cu/CeO_2, the redox process becomes even clearer: *in situ* and operando spectroscopy support a cycle involving Cu^{2+}–O^{2-}–Ce^{4+} and Cu^{+}–O_v–Ce^{3+} ensembles, with $CO_2^{\bullet-}$-type activation and no strong evidence that formate is the primary RWGS intermediate [29].

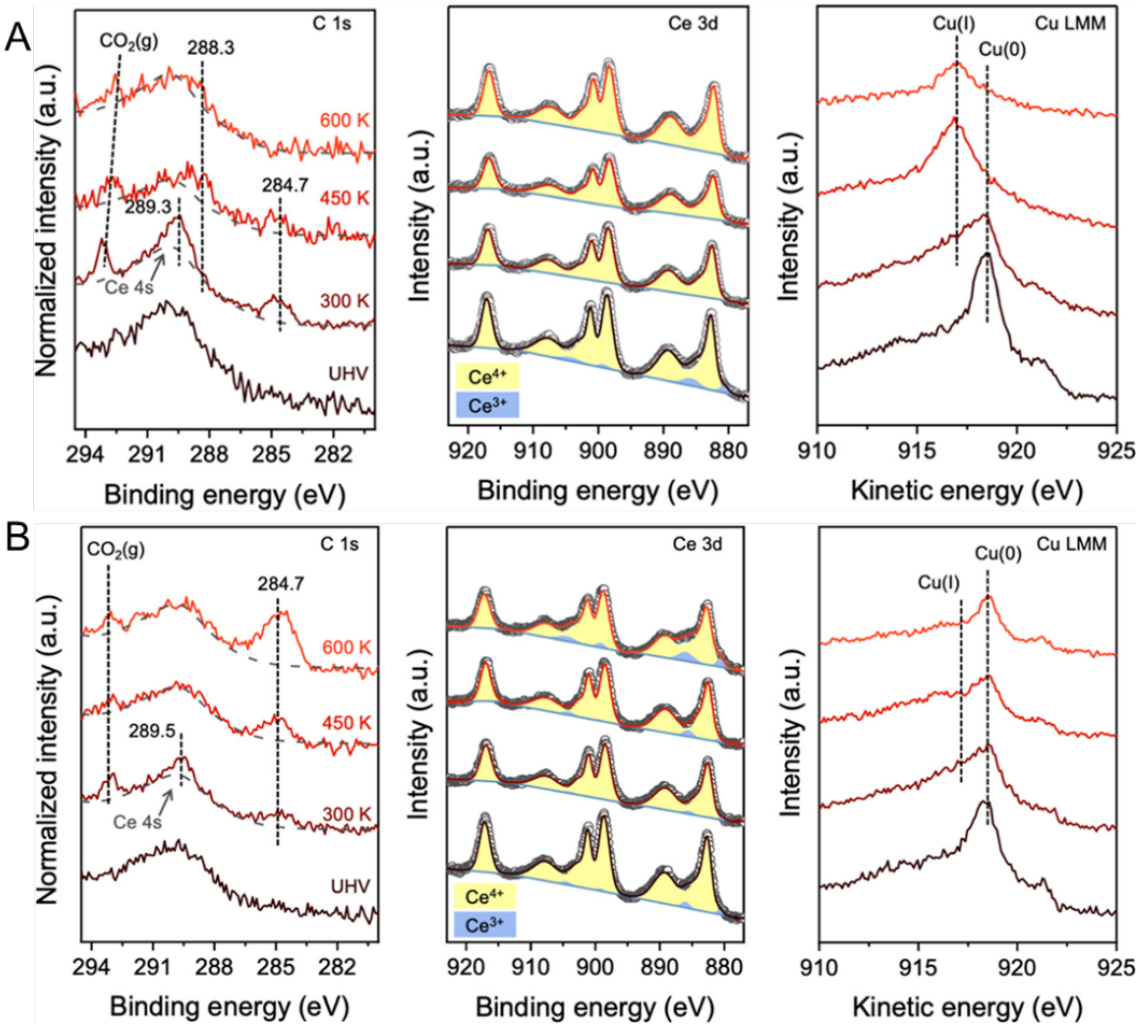

Figure 2. NAP-XPS evidence for the stepwise reconstruction of the Cu/CeO_{2-x} interface during CO_2 activation and subsequent CO_2/H_2 reaction. (**A**) C 1s, Ce 3d, and Cu LMM spectra of the Cu/CeO_{2-x} model surface under UHV and 0.2 mbar of CO_2 at 300, 450, and 600 K. The difference in C 1s peaks for gas-phase CO_2 originates from the different sample-aperture distances, which are optimized for each measurement. (**B**) C 1s, Ce 3d, and Cu LMM spectra of the Cu/CeO_{2-x} model surface under UHV and 0.2 mbar of CO_2 + 0.6 mbar of H_2 at 300, 450, and 600 K. Reproduced with permission [28]. Copyright 2021, American Chemical Society.

The same Cu–CeO_x interface can also be directed away from CO and toward deeper hydrogenation. In W-doped Cu/CeO_2 used for methanol synthesis, *in situ* XANES and DRIFTS showed that W stabilizes a portion of Ce^{3+} that is not strongly redox-active, suppresses RWGS competition, and shifts the chemistry toward a formate/methoxy pathway [71]. A more compositionally complex CuO–ZnO–CeO_2 catalyst reaches a similar conclusion from a morphological perspective, where *in situ* DRIFTS identifies a carbonate-formate-methoxy

sequence on the most defective sample [72]. Even in oxidation chemistry, these same structural principles recur. A hydroxyl-rich $Ce(OH)_x$-derived support results in CuO/CeO_2 with better CuO_x dispersion, more CuO_x–CeO_2 interface, increased defects, and higher oxygen mobility, all of which enhance both CO oxidation and NO reduction by CO [73]. Au/CeO_2 in RWGS offers an instructive contrast to these Cu systems. Operando Raman, UV-vis, and transient DRIFTS showed that subsurface O_vs correlate with activity but are not rate-determining, and the main route is associative, proceeding through carbonate and formate intermediates rather than a purely redox cycle [74].

2.5. Atomically Resolved Active Motifs in Pt/CeO_2 and Au/CeO_2

Pt/CeO_2 and Au/CeO_2 remain the clearest examples where synchrotron-based methods have identified the working interfacial motif almost atom by atom. For Pt/CeO_2 in WGS, combined operando XAS, AP-XPS, DRIFTS, and microscopy revealed that the catalytically relevant interface is a dynamic perimeter Pt^0–O_v–Ce^{3+} ensemble formed under reaction conditions, rather than a static oxidized Pt site [30]. Figure 3 makes this point more directly. In Figure 3a, operando XPS tracks the redistribution of Pt valence states as the catalyst is cooled under WGS conditions, showing that the Pt surface does not remain in a single fixed oxidation state but responds continuously to the reaction environment. Figure 3b shows the corresponding evolution of cerium valence, indicating that the Pt-state changes occur together with a reversible shift in the Ce^{3+}/Ce^{4+} balance at the interface. Taken together, the two panels show that Pt and ceria do not evolve independently. Instead, the perimeter is restructured cooperatively under the reaction mixture, which is why the active motif is better described as a working-state Pt^0–O_v–Ce^{3+} boundary than as a pre-existing PtO_x/CeO_2 contact. This is also the key point that conventional ex situ characterization would miss, because measurements performed only before or after reaction cannot capture the correlated and reversible redistribution of Pt and Ce valence states under WGS conditions [30]. On CeO_2(110), Pt clusters can even become partially embedded in the oxide, generating $Pt^{\delta+}$–O_v–Ce^{3+} motifs that stabilize Pt and lower the barrier for H_2O dissociation [31]. *In situ* XAS then addressed a separate but important question by showing that both Au and Pt stay formally unoxidized during WGS on CeO_2-based catalysts, despite their strong interaction with oxygen-deficient ceria [32]. The size effect in Pt/CeO_2 has now also been quantified. Operando NAP-XPS and kinetic analysis showed that the intrinsic activity of perimeter corner Pt atoms increases sharply below an average particle size of about 1–1.5 nm due to an electronic, not merely geometric effect [33]. Under low-temperature CO oxidation conditions, the distinction between Pt species remains equally significant. On Pt–CeO_2 model catalysts, only systems containing Pt^0 nanoparticles displayed a pronounced low-temperature redox channel, while more ionic Pt species were far less effective below room temperature [34]. A different pathway to high activity was reported for atomically dispersed Pt^{2+}/CeO_2, where high-temperature steam treatment activated lattice oxygen near Pt without destroying the single-atom dispersion, thereby lowering the light-off temperature for CO oxidation [35].

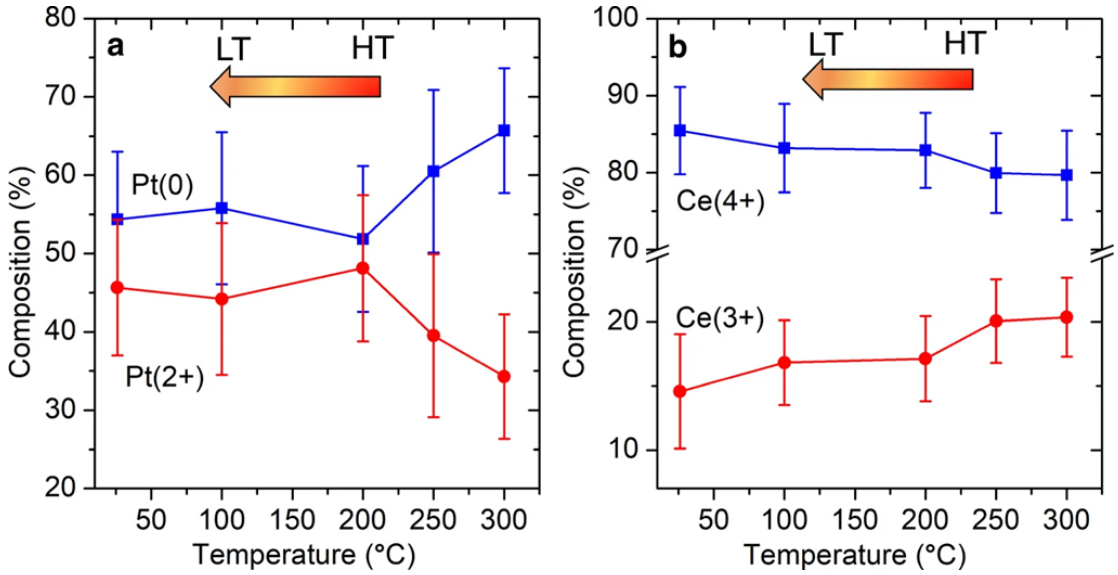

Figure 3. The valence state change of (**a**) Pt and (**b**) Ce under WGS conditions when the temperature drops from 300 °C (HT) to RT (LT). Reproduced with permission [30]. Copyright 2021, Nature Publishing Group.

Au/CeO_2 demonstrates the same support redox chemistry and interfacial electronic heterogeneity. Time-resolved operando XAS at the Ce L_3 edge revealed that the support quickly adjusts its Ce^{3+} population during CO

oxidation and approaches a gas-dependent steady state, largely forgetting the pretreatment history [75]. *In situ* XPS, SRPES, DRIFTS, and DFT analyses showed that ceria-supported Au particles do not have a uniform charge state: Au^{+} is favored at the interface, Au^{0} dominates the particle surface, and $Au^{\delta-}$ can form near O_vs when ceria is partially reduced by CO [76]. On Au/CeO_2(111), the local surface geometry is also important. *In situ* spectroscopy and microscopy demonstrated that step-rich surfaces change the distribution of Au species and, consequently, the CO oxidation mechanism itself [77]. These Pt and Au studies do more than identify active species in specific reactions. They reveal that the CeO_x interface is electronically non-uniform and structurally dynamic, with both features depending on the reaction.

Two additional cases help clarify the therma-catalysis picture. In soot oxidation, ambient-pressure photoemission demonstrated that Ce^{3+} formation and O_vs generation happen directly at the ceria-soot contact, while a second pathway involves reoxidation by gas-phase O_2 and the formation of reactive superoxide/peroxide species on ceria [78]. In methane partial oxidation over CuO–NiO/CeO_2–ZrO_2, *in situ* XANES revealed a clear connection between the redox behavior of Ce and Ni, and the addition of Cu prevented Ni reoxidation and carbon buildup under reaction conditions [79]. These systems differ chemically from CO_2 methanation, RWGS, WGS, or low-temperature CO oxidation, but they support the same conclusion. In thermal catalysis, CeO_x is not just a support that supplies vacancies or disperses metal particles. Its catalytic role involves creating, stabilizing, and reorganizing specific interfacial structures under the chemical potential of the gas mixture used. That is precisely why synchrotron-based XAS, NAP-XPS, RPES, and related operando techniques are so valuable in this field.

3. Photocatalysis

In photocatalysis, interest in CeO_x originates from its high sensitivity of chemical states to the reaction environment [16]. The Ce^{4+}/Ce^{3+} redox couple, the relative ease of O_vs formation, and the participation of defect-derived 4f states enable CeO_2 to serve not only as a semiconductor but also as a chemically responsive interfacial component that can control charge separation and small-molecule activation [80]. However, the wide band gap of pristine ceria and significant carrier recombination greatly limit the direct use of CeO_2 as a standalone photocatalyst. Improved performance typically requires interfacial design, defect engineering, or coupling with another component [36,81,82]. Against this background, the central issue in CeO_x photocatalysis is not just enhancing light absorption, but also identifying the true interfacial structure formed under illumination that is connected to catalytic activity.

3.1. Hydrogen-Related Photocatalysis

This issue is already evident in hydrogen-related reactions. In ternary Pt–CeO_2–TiO_2 catalysts for thermo-photo H_2 production, the combined effect of heat and light produced a measurable synergistic response, and *in situ* micro-XAS along with DRIFTS showed that ceria directly participates in the working-state sequence of methanol activation, decarbonylation, water-gas shift chemistry, and H_2 evolution [36]. In CeO_2/MXene heterojunctions, the MXene phase promotes interfacial electron transfer and increases H_2 evolution compared to bare CeO_2, indicating that the contribution of ceria in such systems heavily relies on charge extraction at the interface [81]. A similar conclusion was drawn from studies on vacancy-engineered CeO_2 nanosheets in photocatalytic water oxidation, where spectroscopic analysis and theoretical calculations linked O_vs to longer carrier lifetimes and a lower barrier for O–O bond formation [82]. Taken together, these studies indicate that the photocatalytic function of CeO_x is determined by the coupling of interfacial charge transfer and surface redox processes under working conditions.

3.2. Illuminated CeO_x Interfaces in CO_2 Photoreduction

The same point becomes clearer in CO_2 photoreduction. In vacancy-rich H–CeO_2, surface O_vs favor methanol formation, while the addition of highly dispersed Ag generates an Ag–O–Ce^{3+} atomic interface that redistributes charge among Ag, lattice oxygen, and reduced cerium. This shifts the surface intermediate network toward acetone formation via a tandem pathway involving C–C coupling. As shown in Figure 4, the *in situ* DRIFTS results reveal a clear progression in CO_2 adsorption behavior from CeO_2 to H–CeO_2 and then to 0.3%Ag/H–CeO_2. CeO_2 mainly displays typical carbonate-type surface species, indicating limited activation of adsorbed CO_2. After reduction, H–CeO_2 shows stronger adsorption features, supporting the role of O_vs in improving CO_2 uptake. Conversely, 0.3%Ag/H–CeO_2 not only sustains stronger adsorption but also forms carboxylate-related species, suggesting that the Ag–O–Ce^{3+}/oxygen-vacancy interface alters the adsorption configuration of CO_2 and stabilizes more reactive surface intermediates. These results suggest that O_vs mostly boost adsorption, while the defect-rich Ag–ceria interface further enhances CO_2 activation [83].

A different interfacial configuration was identified for atomically dispersed Ni on CeO_2 under concentrated solar irradiation, where XAS showed oxidized single-site Ni, valence-band XPS indicated an increased Ce^{3+} population during operation, and the catalyst achieved highly selective methane formation from CO_2 and H_2O [84]. In Zn_2GeO_4@CeO_2 core@shell nanorods, XPS and Mott-Schottky analysis supported the formation of a type-I junction, while *in situ* FT-IR revealed that the CeO_2 shell changed the adsorbed intermediate network and enhanced CO selectivity [85]. These results suggest that the role of CeO_x in CO_2 photoreduction is determined by the electronic structure of the illuminated interface rather than just the nominal presence of ceria or vacancies alone [83].

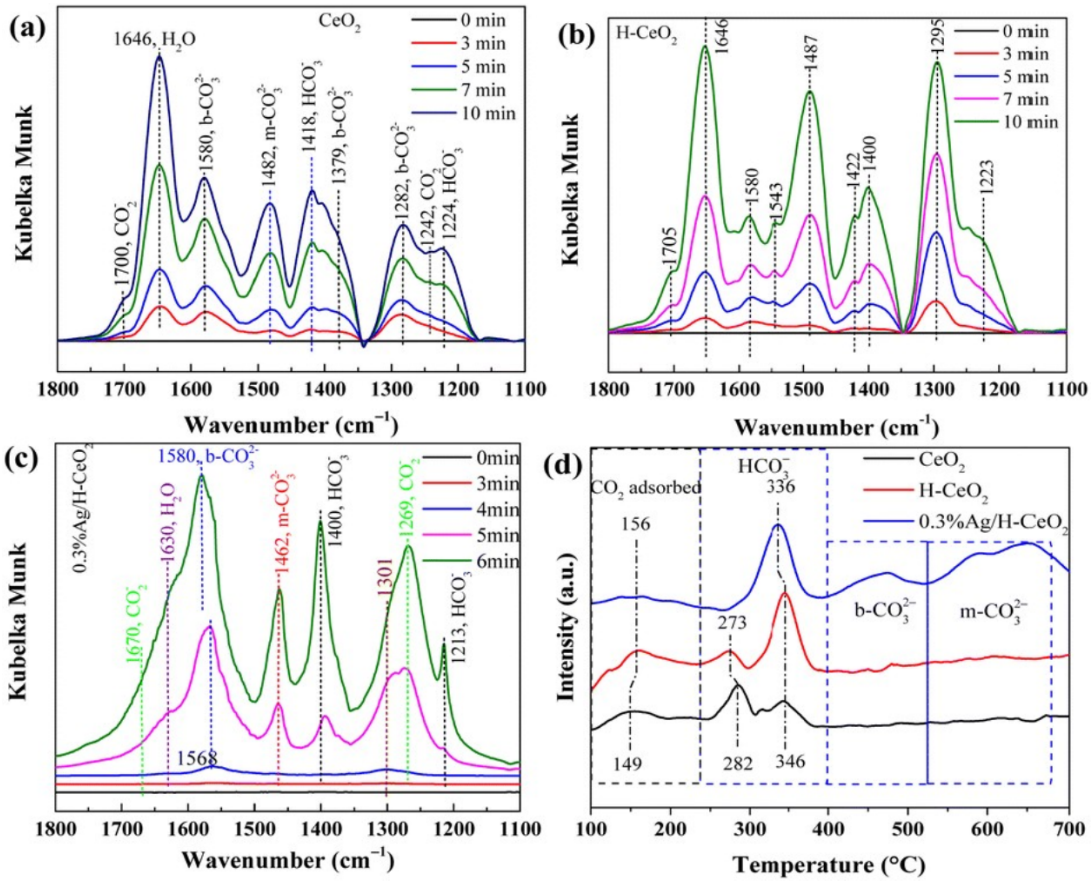

Figure 4. *In situ* DRIFTS of CO_2 adsorption (**a**–**c**) on different photocatalysts (**a**): CeO_2; (**b**): H–CeO_2; (**c**): 0.3%Ag/H–CeO_2), and the CO_2-TPD plots adsorbed on different photocatalysts (**d**). Reproduced with permission [83]. Copyright 2023, Royal Society of Chemistry.

3.3. Vacancy-Derived Ce^{3+} Sites in Photocatalytic C–N Coupling

The role of vacancy-derived Ce^{3+} sites becomes even clearer in photocatalytic C–N coupling. In mesoporous CeO_{2-x} nanorods created by reductive treatment, XPS, EXAFS, and EELS confirmed the presence of reduced cerium and local structural changes related to vacancy formation, while FT-IR, LC-MS, and DFT showed that these defect sites facilitated the co-adsorption and activation of N_2 and CO_2, increased electron donation from Ce 4f states into N_2 antibonding orbitals, reduced the free-energy barrier for CO_2 reduction in the presence of activated nitrogen, and stabilized the key *NCON intermediate over the competing *NNH pathway. This enables the formation of urea [86]. This finding is significant because it demonstrates that O_vs in CeO_x not only enhance adsorption or suppress recombination, but can also reorganize the reaction pathway toward interfacial coupling chemistry.

A substantial part of the recent CeO_x photocatalysis literature lies in the transition region between photocatalysis and photothermal catalysis, where working-state surface chemistry can often be followed more directly. In phosphated Ni–CeO_2 nanorod heterostructures for hybrid photocatalytic dry reforming, phosphate species increased surface basicity, improved CO_2 adsorption, and helped stabilize smaller Ni clusters, while *in situ* DRIFTS showed that illumination altered the distribution of adsorbed intermediates rather than acting only through bulk heating [37]. A more explicit picture was obtained for Ni/CeO_{2-x} catalysts prepared by non-oxidative calcination, where operando DRIFTS, *in situ* Raman, XAS, UV-vis spectroscopy, and DFT consistently identified Ni–O_v–Ce^{3+} motifs as the active interfacial sites under thermal and photo-thermal dry reforming conditions [38]. Under irradiation, therefore, the operative CeO_x interface should be described as a dynamically reconstructed

boundary containing reduced cerium, O_vs, adsorbates, and metal sites, rather than as a static combination of support and nanoparticle.

The same conclusion also applies to photothermal CO_2 hydrogenation. In Ni-loaded CeO_2 nanocrystals with inherited structural characteristics, abundant O_vs and surface hydroxyls on CeO_2 generated numerous frustrated-Lewis-pair-like sites for CO_2 adsorption and activation, while strong Ni–ceria interaction promoted H_2 dissociation and H spillover, leading to high CH_4 productivity and near-complete methane selectivity [87]. At the other extreme of product selectivity, pure CeO_2 in photothermal RWGS produced CO through a vacancy-mediated redox mechanism rather than through an associative formate route, and the combination of transient measurements, *in situ* XPS, pseudo *in situ* electron paramagnetic resonance (EPR), and operando DRIFTS supported a Ce^{4+}–O–Ce^{4+} ⇌ Ce^{3+}–O_v–Ce^{3+} redox cycle under reaction conditions [39]. As shown in Figure 5, the *in situ* Ce 3d XPS results under steady-state and transient conditions indicate that illumination maintains a higher Ce^{3+} population on CeO_2 and facilitates the regeneration of reduced Ce^{3+}–O_v–Ce^{3+} pairs, while the transient RWGS response shows that CO is formed during exposure of the reduced surface to CO_2 rather than during H_2 feeding [39]. Taken together, these results provide direct working-state evidence that the photothermal RWGS reaction on CeO_2 proceeds through cyclic reduction of Ce^{4+} sites by H_2 and reoxidation of vacancy-containing Ce^{3+} sites by CO_2.

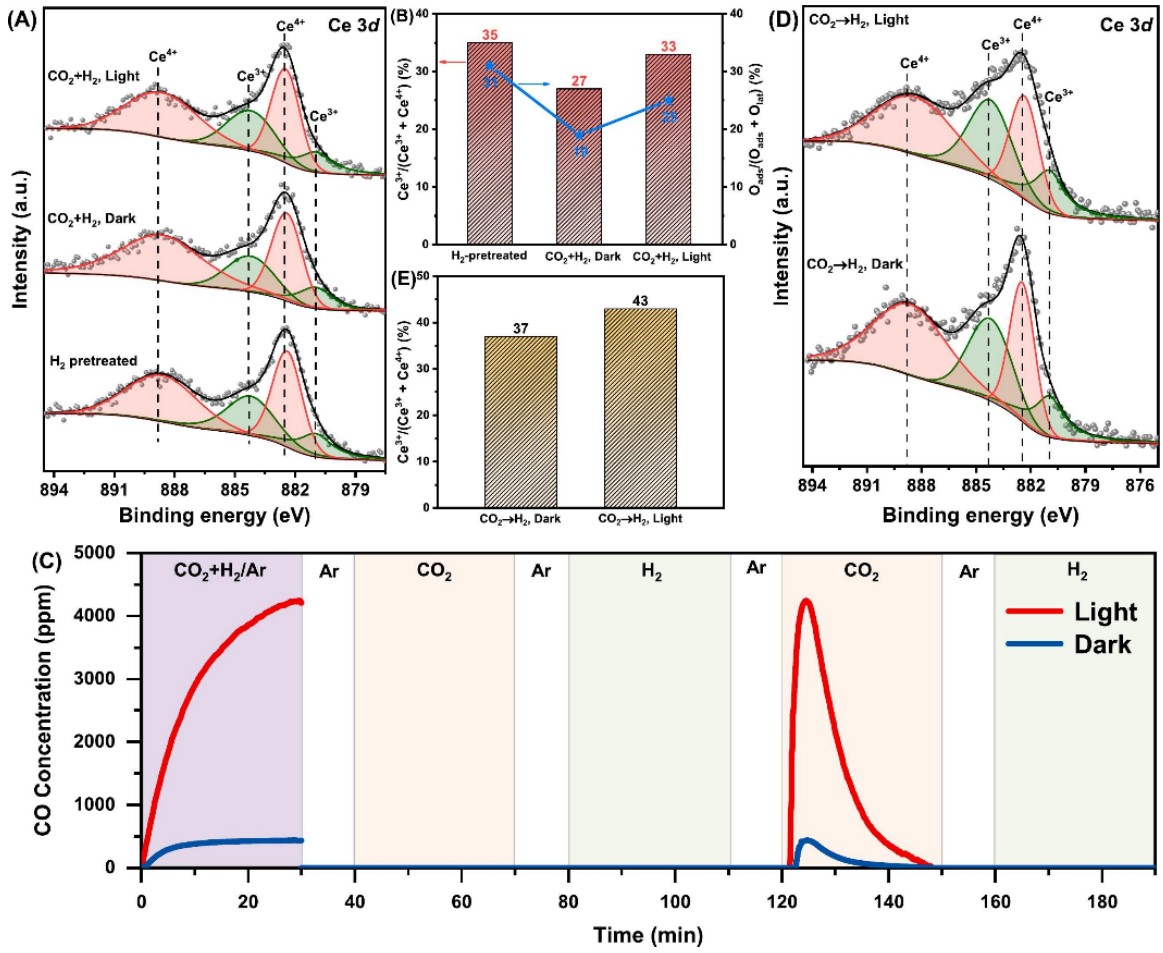

Figure 5. (**A**) Ce 3d *in situ* XPS spectra of CeO_2 under light and dark conditions at 400 °C. (**B**) Concentrations of Ce^{3+} and O_{ads} species in Ce 3d and O 1s *in situ* XPS spectra of CeO_2. (**C**) Transient RWGS reaction on CeO_2 (150 mg) in a fixed-bed flow reactor under both dark and 1.8 W/cm2 light conditions at 400 °C: Time course of CO concentration (determined by a gas analyzer) under CO_2 + H_2 and followed a cyclic feed of 5%CO_2→Ar→5%H_2. Reaction conditions of CO_2 + H_2 co-feeding: 1%CO_2, 4%H_2, Ar balance, and total flow rate of 50 mL min^{-1}. (**D**) Ce 3d *in situ* XPS spectra of CeO_2 under light and dark conditions at 400 °C. (**E**) Concentrations of Ce^{3+} species in Ce 3d *in situ* XPS spectra of CeO_2 from Figure 5D. Reproduced with permission [39]. Copyright 2025, Elsevier.

Overall, the main advancement in recent CeO_x photocatalysis is not simply in adding vacancies, heterojunctions, or atomically dispersed metals [36,38,39,84,86]. The more important development is that these structural features are now being observed under working or near-working conditions, rather than just inferred from ex situ characterization [81–83,85]. This area remains less developed than thermal catalysis because many

studies still rely primarily on ex situ XPS, optical characterization, and post-reaction structural analysis, especially in composite and photothermal systems [37,87]. Nonetheless, the key point is now clear: catalytic behavior in CeO_x photocatalysis depends on the actual interfacial features formed under illumination, including the Ce^{3+}/Ce^{4+} ratio, the creation and healing of O_vs, the stabilization of adsorbate-metal-oxygen-cerium linkages, and the connection of these features to charge transfer and elementary reaction steps [39,83,84]. This is exactly the level of detail where synchrotron-based X-ray spectroscopy can provide its most valuable insights in future studies of CeO_x interfaces in model photocatalytic systems [36,38,86].

4. Electrocatalysis

Electrocatalysis places a stricter demand on the structural description of CeO_x interfaces than thermal catalysis, because the active state is created under bias rather than simply inherited from the as-prepared material. In Cu–CeO_2, CeO_2–SnO_2, and CoO_x/CeO_2 systems, operando or *in situ* measurements consistently show that the oxidation state of the metal component, the density of O_vs, and the role of the CeO_x phase all evolve during reaction, so the precursor structure is only a starting point for mechanistic analysis [40,41]. Accordingly, the key question is not whether CeO_x is present, but how Ce^{3+}/Ce^{4+} interconversion, vacancy formation, and interfacial charge transfer redistribute the elementary steps of CO_2 reduction, water splitting, and related biomass conversions under working conditions [42,43].

4.1. Cu-Based CO_2 Reduction Targeting C_{2+} and Methane Selectivity

In Cu-based CO_2 reduction, the most direct effect of CeO_2 is to stabilize Cu states that are otherwise difficult to maintain under cathodic polarization. By tuning the CuO–CeO_2 interfacial structure, Chu et al. showed that Cu^+ could be retained during electrolysis and that the ethylene faradaic efficiency increased to 50.0%; DFT further indicated that Cu^+ is preferentially formed at the CuO–CeO_2 boundary [44]. Yan et al. extended this picture under flow-cell conditions and, using operando XAS and *in situ* Raman, showed that the CeO_2/Cu interface and subsurface Cu_2O coexist during CO_2RR [41]. In that system, CeO_2 did not simply increase the number of Cu sites. Rather, it changed the reaction network by facilitating water activation near the oxide and lowering the thermodynamic and kinetic cost of *CO hydrogenation to *CHO, which in turn promoted C–C coupling and raised the C_{2+} faradaic efficiency to 75.2% [41]. Direct operando XAS evidence for this working-state regulation is shown in Figure 6, where the Cu K-edge evolution indicates the emergence of low-valent Cu species under CO_2RR conditions, while the Ce L_3-edge remains nearly unchanged, consistent with a stabilizing interfacial role of CeO_2 rather than direct participation of Ce redox cycling in the catalytic step.

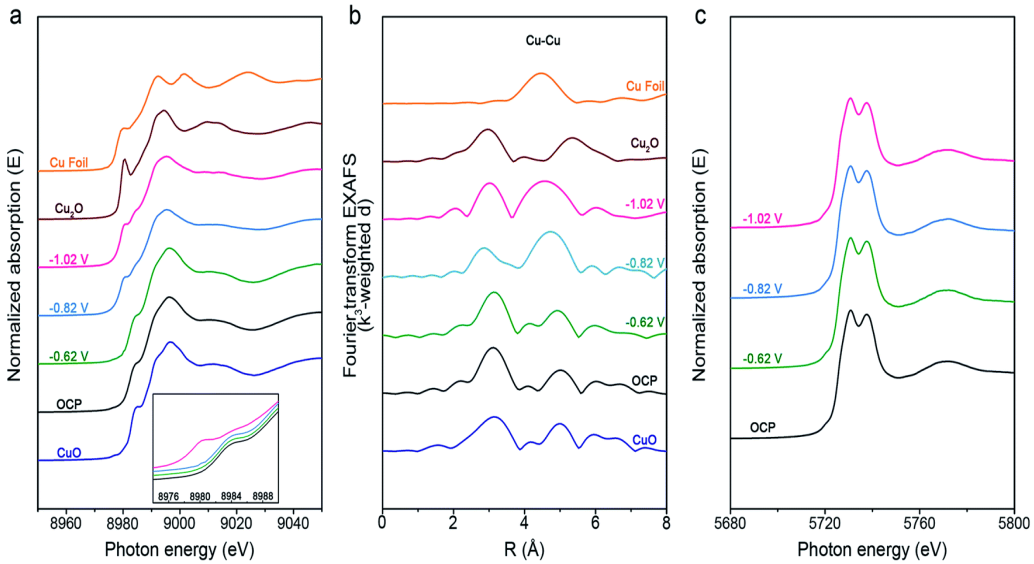

Figure 6. (**a**,**b**) Operando XANES and the corresponding Fourier transforms of k^3-weighted EXAFS data at the Cu K-edge (**c**) Operando XANES at the Ce L_3-edge at various applied potentials during CO_2RR. Reproduced with permission [41]. Copyright 2021, Royal Society of Chemistry.

The same CeO_x chemistry can also shift Cu catalysts away from C_{2+} formation and toward methane when the interfacial structure favors sequential hydrogenation over carbon-carbon coupling. On Cu/CeO_2, Patra et al.

correlated the highest CH_4 selectivity with Cu^+–O_v–Ce^{3+} motifs and used *in situ* Raman that hydroxylated surfaces and a high local pH assist the protonation steps required for deep reduction [42]. A complementary mechanistic study on Cu/CeO_2 nanorods reached a similar conclusion from a different angle: quasi *in situ* ATR-FTIR, *in situ* DRIFTS, and theory supported a pathway in which Cu insertion into ceria lowers the barrier from *CO_2 to *COOH and drives *CHOH toward *CH rather than *CH_2OH, thereby favoring methane formation [43]. This methane-selective regime becomes even clearer in a model catalyst based on ultrasmall CeO_2 clusters loaded with Cu single atoms. In that system, *in situ* synchrotron-radiation FTIR detected *COOH, *CO, and *CHO intermediates, and the isolated Cu sites were shown to suppress C–C coupling while promoting the hydrogenation sequence toward CH_4 [44]. Taken together, these studies indicate that CeO_x does not impose one universal CO_2RR selectivity pattern on Cu. Its effect depends on whether the working interface preferentially stabilizes Cu sites for *CHO generation and further hydrogenation, or Cu ensembles that can continue toward C–C coupling [41–44].

4.2. Non-Cu CO_2RR Pathways Regulated by CeO_x Interfaces

CeO_x also creates distinct interfacial motifs in non-Cu CO_2RR catalysts. In Ag_1/CeO_2, each Ag single atom is associated with interfacial O_vs, producing Ag–O–Ce^{3+} atomic interfaces that activate neighboring Ce–O units for CO_2 adsorption and lower the barrier for *COOH–to–CO conversion [88]. In a different product channel, hybridization of Bi_2O_3 with CeO_x improved formate production because defective CeO_x assisted both CO_2 activation and water dissociation, generating H for the rate-determining hydrogenation step while still disfavoring H_2 evolution [89]. An even stronger example of a dynamic oxide-mediated mechanism was reported for CeO_2–SnO_2. There, *in situ* attenuated total reflection infrared absorption spectroscopy (ATR-IRAS), operando Raman, and post-reaction XPS supported a CeO_2-mediated $Sn^0/Sn^{\delta+}$ redox cycle in which O_vs on ceria promote water dissociation to generate *OH and *H; the former reoxidizes Sn^0 to the formate-active $Sn^{\delta+}$ state, while the latter assists formation of the key *OCHO intermediate [90]. In these systems, CeO_x is therefore not best described as a passive support. It actively shapes the proton supply, the preferred adsorbate geometry, and, in some cases, the redox regeneration of the metal site itself [88–90].

4.3. CeO_x Interfaces in OER, HER, and Biomass Electrooxidation

The anodic role of CeO_x is different. In OER, CeO_x more often functions as an interfacial regulator of transition-metal redox chemistry than as the direct oxygen-evolving center. Early synchrotron photoemission work on CeO_x/CoO_x showed that Ce perturbs the electronic structure of surface Co species and facilitates CoOOH formation, while DFT suggested that the modified interface weakens the binding of oxygenated intermediates relative to bare Co_3O_4 [45]. In acidic media, this role becomes more clearly defined. Huang et al. combined *in situ* Raman with ex situ XAS and showed that nanocrystalline CeO_2 modifies the local bonding environment in Co_3O_4, allowing CoIII surface species to be oxidized more readily to OER-active CoIV and suppressing the charge accumulation and extensive surface reconstruction observed for Co_3O_4 alone [46]. Operando hard XAS then sharpened this mechanistic separation: in CoO_x/CeO_2, the Co K edge changed with potential, whereas the Ce L_3 edge remained essentially unchanged throughout the OER region, showing that CeO_2 is not the redox-active OER center under these conditions [47]. What CeO_2 does change is the electronic structure of the CoO_x surface, the flat-band potential, and the way the Co oxidation state evolves under bias, all of which can alter the preferred OER pathway [47]. This mechanistic distinction is directly illustrated in Figure 7. During operando hard X-ray absorption spectroscopy (hXAS) measurements, the Co K-edge shifts markedly with increasing anodic potential for both CoO_x and CoO_x/CeO_2, confirming that Co is the redox-responsive component under OER conditions. In contrast, the Ce L_3-edge of CoO_x/CeO_2 remains nearly unchanged throughout the OER region. Moreover, the smaller ΔE edge of the Co K-edge in CoO_x/CeO_2 relative to CoO_x indicates that CeO_2 modifies the evolution of the Co working state rather than acting as the primary redox-active OER center [47].

A related effect is found in RuO_2–CeO_2 heterostructures under acidic OER conditions. *In situ* ATR-SEIRAS identified both *OOH and *O–O species on RuO_2–CeO_2, whereas RuO_2 alone showed only the adsorbate pattern expected for the adsorbate evolution mechanism. Combined with isotope-labeling DEMS, these measurements suggest that the RuO_2–CeO_2 interface opens an additional reaction pathway that is absent on noninterfacial RuO_2 sites. At the same time, the heterostructure suppresses Ru dissolution during long-erm operation, indicating that the CeO_2 phase is involved not only in activity enhancement but also in stabilizing the working Ru environment [48]. These OER studies collectively show that the value of CeO_x lies in how it reshapes the redox landscape and adsorption energetics of the actual metal-centered active phase, rather than in serving as an autonomous catalytic center [45–48].

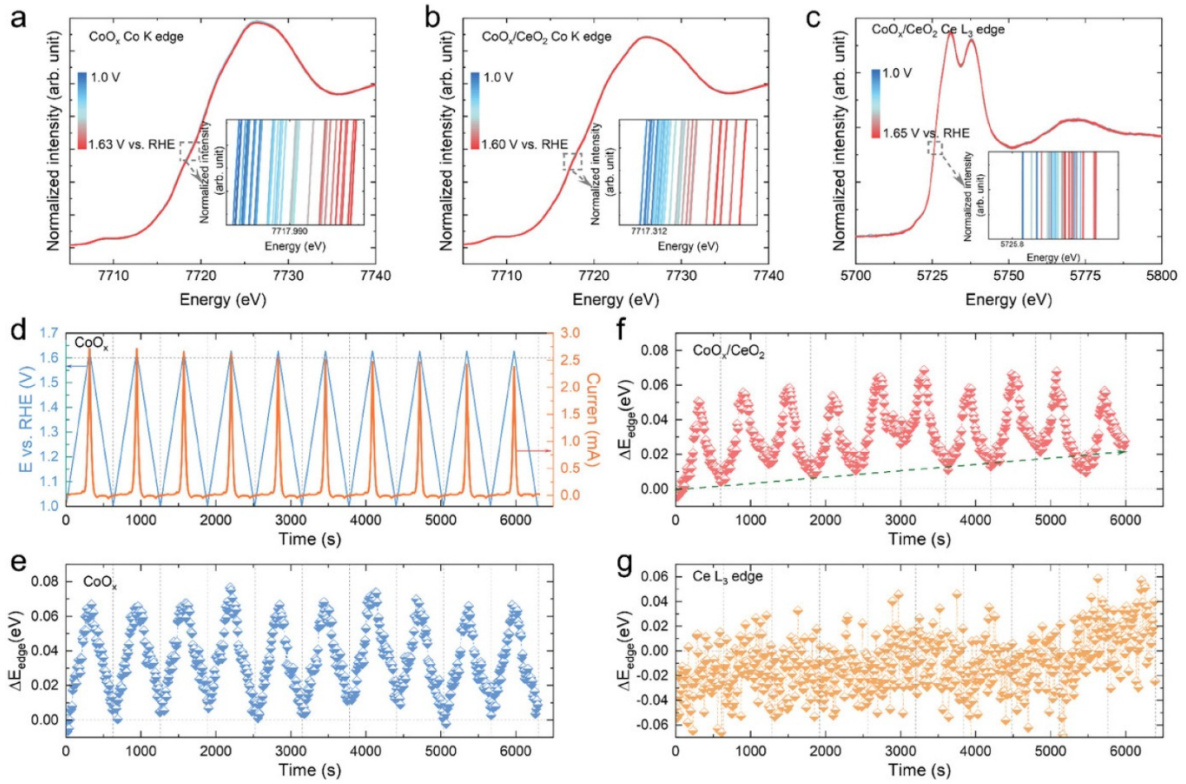

Figure 7. Operando hXAS characterizations on CoO_x and CoO_x/CeO_2 to monitor the evolution of Co K edge and Ce L_3 edge during CV measurement with a scan rate of 2 mV s^{-1}. The XANES spectra at the (**a**) Co K edge of CoO_x; (**b**) Co K edge of CoO_x/CeO_2 and (**c**) Ce L_3 edge of CoO_x/CeO_2 during the first anodic scan. Insets in panel (**a**–**c**) highlights the shift in absorption edge. (**d**) The applied potential and the OER current of CoO_x electrode as a function of time during the 10 CV cycles of the operando hXAS characterization. The corresponding energy shift (ΔE edge) at the Co K edge spectra for (**e**) CoOx and (**f**) CoO_x/CeO_2 during 10 CV cycles. (**g**) The ΔE edge at the Ce L_3 edge spectra for the CoO_x/CeO_2. The ΔEedge in panel (**e**–**g**) was obtained by comparing the energy of absorption edge (Eedge) at the specific potential to that at 1.0 V versus RHE during first anodic scan. Reproduced with permission [47]. Copyright 2024, Wiley-VCH.

For HER, the main contribution of CeO_x is to accelerate water activation while tuning hydrogen binding at the neighboring conductive phase. In O_vs-rich CeO_2/Co_4N, experimental characterization together with DFT showed that vacancy-containing Ce sites adsorb water more strongly and promote its dissociation, whereas interfacial electron transfer optimizes the hydrogen adsorption free energy on Co_4N, improving both the Volmer-Heyrovsky steps [91]. Zhou et al. later described CeO_2 in Co_4N@CeO_2 as an "electron pump", emphasizing that electrons are transferred from Co_4N to CeO_2 and that this redistribution lowers the water dissociation barrier, brings ΔG*H closer to thermoneutrality, and modifies the OER potential-determining step at the same heterointerface [92]. Although the language differs between the two studies, the mechanistic conclusion is consistent: in alkaline HER, CeO_x helps by separating the roles of water cleavage and hydrogen recombination across a heterogeneous interface rather than forcing both to occur with equal efficiency on a single site [91,92].

The same interfacial logic extends to electrochemical biomass conversion. In Co_3O_4/CeO_2 for HMF oxidation, *in situ* electrochemical impedance spectroscopy established a structure-activity-potential relationship and showed that the heterointerface facilitates both charge transfer and the structural evolution of the electrode during reaction [93]. DFT in the same study indicated that CeO_2 moderates the adsorption strengths of HMF and OH* and lowers the reaction energy associated with dehydrogenation, which is consistent with the improved FDCA yield and faradaic efficiency [93]. Under cathodic conditions, a Cu–CeO_2 foam used for HMF hydrogenation shows a similarly dynamic behavior. *In situ* XANES and post-reaction characterization indicated that the catalyst evolves during operation, with Cu particles forming on a partially reduced CeO_2 coating; this combination improves conductivity and provides the sites responsible for selective BHMF formation [94]. These non-CO_2 examples are useful because they reinforce the same mechanistic point seen in CO_2RR and HER: the catalytically relevant CeO_x interface is generally the bias-generated state, not the structure drawn from the synthesis section [93,94].

Overall, the electrocatalysis literature does not support a single, fixed role for CeO_x. What emerges instead is a more specific and more useful description. Under cathodic bias, CeO_x commonly stabilizes defect-rich interfacial motifs that enhance water activation, maintain unusual metal valence states, and redirect hydrogenation pathways [40,42,90]. Under anodic bias, it more often tunes the redox response and adsorption energetics of adjacent transition-metal sites without becoming the primary oxygen-evolving center [46–48]. For a spectroscopy-centered review, this distinction matters. The central advance is not simply that CeO_x improves performance, but that operando XAS, *in situ* vibrational spectroscopy, and related methods now make it possible to resolve when, where, and in what electronic form the CeO_x interface actually participates in electrocatalysis [41,47,90].

5. Conclusions

The central issue in CeO_x-based model catalysis isn't just identifying a support phase, but understanding the interfacial structure formed during operation. In thermal catalysis, photocatalysis, and electrocatalysis, the most important catalytic structures form under working conditions and are often located at dynamic interfaces. These interfaces host processes like oxygen-vacancy formation and refill, Ce^{4+}/Ce^{3+} interconversion, charge transfer, and adsorbate-induced restructuring occur simultaneously. Therefore, CeO_x is better viewed as an active interfacial component rather than a passive support because it stabilizes reaction-specific motifs that govern bond activation, hydrogen transfer, oxygen exchange, and product selectivity.

The comparison among the three catalytic fields also shows that the role of CeO_x is strongly influenced by the reaction environment. In thermal catalysis, operando XAS, AP-XPS, RPES, and *in situ* vibrational methods have already demonstrated that active structures often involve vacancy-rich metal-ceria perimeter sites, mixed ionic/metallic interfacial states, and dynamically changing reduced ceria environments. In photocatalysis, the same working-state perspective is developing, but many assignments still rely heavily on ex situ defect analysis or indirect optical signatures. In electrocatalysis, the requirement is even stricter because the active interface is formed under bias and may differ significantly from the precatalyst.

From a spectroscopic standpoint, recent advances not only demonstrate that CeO_x can boost catalytic performance but also enable the identification of when CeO_x participates directly, in what structural and electronic form it does so, and how that participation evolves during catalysis. Simultaneously, the field still needs a more quantitative understanding of working CeO_x interfaces. Future progress depends on linking spectroscopic signatures to the concentration, location, and lifetime of specific interfacial motifs, and then connecting those motifs more directly to fundamental reaction steps. The next step is therefore not just to identify reduced or defective CeO_x, but to determine which specific interfacial structures are formed under given conditions, how stable they are, and which catalytic functions they actually control.

Author Contributions

F.S.: conceptualization, writing—review & editing; J.X.: writing-original draft; W.S.: investigation; Z.L.: investigation; H.W.: conceptualization, writing-review & editing. L.X.: conceptualization, writing—original draft; J.M.: conceptualization, writing—review &editing; B.M.: conceptualization, writing—review & editing. All authors have read and agreed to the published version of the manuscript.

Funding

This work was financially supported by the National Key Research and Development Program of China (2021YFA1600802) and the Photon Science Center of Chinese Academy of Science.

Institutional Review Board Statement

Not applicable.

Informed Consent Statement

Not applicable.

Data Availability Statement

Not applicable.

Conflicts of Interest

The authors declare no competing financial interests.

Use of AI and AI-Assisted Technologies

During the preparation of this work, the authors used ChatGPT to improve language. After using this tool, the authors reviewed and edited the content as needed and take full responsibility for the content of the published article.

References

1. Ziemba, M.; Schilling, C.; Ganduglia-Pirovano, M.V.; et al. Toward an Atomic-Level Understanding of Ceria-Based Catalysts: When Experiment and Theory Go Hand in Hand. *Acc. Chem. Res.* **2021**, *54*, 2884–2893.
2. Mullins, D.R. The Surface Chemistry of Cerium Oxide. *Surf. Sci. Rep.* **2015**, *70*, 42–85.
3. Wang, X.; Wang, J.; Sun, Y.; et al. Recent Advances and Perspectives of CeO_2-Based Catalysts: Electronic Properties and Applications for Energy Storage and Conversion. *Front. Chem.* **2022**, *10*, 1089708.
4. Garcia, X.; Soler, L.; Divins, N.J.; et al. Ceria-Based Catalysts Studied by Near Ambient Pressure X-ray Photoelectron Spectroscopy: A Review. *Catalysts* **2020**, *10*, 286.
5. Yang, C.; Yu, X.; Heißler, S.; et al. Surface Faceting and Reconstruction of Ceria Nanoparticles. *Angew. Chem. Int. Ed.* **2017**, *56*, 375–379.
6. Lykhach, Y.; Kozlov, S.M.; Skála, T.; et al. Counting Electrons on Supported Nanoparticles. *Nat. Mater.* **2016**, *15*, 284–288.
7. Lykhach, Y.; Figueroba, A.; Farnesi Camellone, M.; et al. Reactivity of Atomically Dispersed Pt^{2+} Species towards H_2: Model Pt–CeO_2 Fuel Cell Catalyst. *Phys. Chem. Chem. Phys.* **2016**, *18*, 7672–7679.
8. Lykhach, Y.; Johánek, V.; Neitzel, A.; et al. Redox-Mediated C–C Bond Scission in Alcohols Adsorbed on CeO_{2-x} Thin Films. *J. Phys. Condens. Matter* **2022**, *34*, 194002.
9. Guda, A.A.; Bugaev, A.L.; Kopelent, R.; et al. Fluorescence-Detected XAS with Sub-Second Time Resolution Reveals New Details about the Redox Activity of Pt/CeO_2 Catalyst. *J. Synchrotron Radiat.* **2018**, *25*, 989–997.
10. Kuan, W.-F.; Chung, C.-H.; Lin, M.M.; et al. Activation of Carbon Dioxide with Surface Oxygen Vacancy of Ceria Catalyst: An Insight from *In Situ* X-ray Absorption Near Edge Structure Analysis. *Mater. Today Sustain.* **2023**, *23*, 100425.
11. Xu, J.-Y.; Sun, W.; Liang, Z.-F.; et al. Artificially Tuning the Population of Ce^{3+} on the Cerium Oxide Surface toward Model Catalytic Reactions. *J. Phys. Chem. C* **2025**, *129*, 21613–21621.
12. Liang, Z.-F.; Xu, J.-Y.; Xie, L.; et al. A Dedicated Beamline for Wide-Energy-Range X-ray Spectroscopy at SSRF: Combining Soft and Hard X-ray Capabilities. *J. Synchrotron Radiat.* **2026**, *33*, 523–530.
13. Mei, B.-B.; Wang, L.-X.; Gu, S.-Q.; et al. A Seven-Crystal Spectrometer for High-Energy Resolution X-ray Spectroscopy at Shanghai Synchrotron Radiation Facility. *Nucl. Sci. Tech.* **2024**, *35*, 156.
14. Xu, Z.; Mao, J.; Mei, B.; et al. Quantitatively Unveiling the Effect of Mass Transfer on CO_2RR through Operando EXAFS and HERFD-XAFS. *Sci. China Chem.* **2025**, *68*, 2044–2050.
15. Ebrahimi, P.; Kumar, A.; Khraisheh, M.A. A Review of CeO_2 Supported Catalysts for CO_2 Reduction to CO through the Reverse Water Gas Shift Reaction. *Catalysts* **2022**, *12*, 1101.
16. Yan, Y.-Q.; Wu, Y.-Z.; Wu, Y.-H.; et al. Recent Advances of CeO_2-Based Composite Materials for Photocatalytic Applications. *ChemSusChem* **2024**, *17*, e202301778.
17. Zhang, H.; Wang, Y.; Song, D.; et al. Cerium-Based Electrocatalysts for Oxygen Evolution/Reduction Reactions: Progress and Perspectives. *Nanomaterials* **2023**, *13*, 1921.
18. López-Rodríguez, S.; Davó-Quiñonero, A.; Bailón-García, E.; et al. Monitoring by *in situ* NAP-XPS of Active Sites for CO_2 Methanation on a Ni/CeO_2 Catalyst. *J. CO_2 Util.* **2022**, *60*, 101980.
19. Barreau, M.; Salusso, D.; Li, J.; et al. Ionic Nickel Embedded in Ceria with High Specific CO_2 Methanation Activity. *Angew. Chem. Int. Ed.* **2023**, *62*, e202302087.
20. Barreau, M.; Salusso, D.; Zhang, J.; et al. Thermal Activation and Deactivation of Ni-Doped Ceria Catalysts in CO_2 Methanation. *Small Sci.* **2025**, *5*, 2400540.
21. Assis, M.S.; Lucas, M.A.; Briois, V.; et al. *In situ* Evaluation of Ni/CeO_2 Catalysts Synthesized via Polymeric Precursor Method by XAS for CO_2 Reduction. *Appl. Catal. B Environ. Energy* **2025**, *369*, 125144.
22. Kenyotha, K.; Kidkhunthod, P.; Poo-arporn, Y.; et al. Ceria-Supported Ni Catalyst with High Catalytic Activity, Selectivity and Stability for CO_2 Conversion to CH_4 by Hydrogenation Reaction Investigated by X-ray Absorption Spectroscopy. *J. Phys. Chem. Solids* **2024**, *190*, 112009.
23. Lucas, M.A.; Lisboa-Filho, P.N.; Possato, L.G. Sonochemical Defect Engineering for Sustainable CO_2 Methanation over Ni/CeO_2 Catalysts with Mechanistic Insights from Operando Studies. *ChemistrySelect* **2025**, *10*, e202504855.

24. Wang, X.; Rodriguez, J.A.; Hanson, J.C.; et al. *In Situ* Studies of the Active Sites for the Water Gas Shift Reaction over Cu–CeO_2 Catalysts: Complex Interaction between Metallic Copper and Oxygen Vacancies of Ceria. *J. Phys. Chem. B* **2006**, *110*, 428–434.
25. Yao, S.Y.; Xu, W.Q.; Johnston-Peck, A.C.; et al. Morphological Effects of the Nanostructured Ceria Support on the Activity and Stability of CuO/CeO_2 Catalysts for the Water-Gas Shift Reaction. *Phys. Chem. Chem. Phys.* **2014**, *16*, 17183–17195.
26. Zhang, Y.; Liang, L.; Chen, Z.; et al. Highly Efficient Cu/CeO_2-Hollow Nanospheres Catalyst for the Reverse Water-Gas Shift Reaction: Investigation on the Role of Oxygen Vacancies through *in situ* UV-Raman and DRIFTS. *Appl. Surf. Sci.* **2020**, *516*, 146035.
27. Ziemba, M.; Hess, C. Unravelling the Mechanism of CO_2 Activation over Low-Loaded Cu/CeO_2(111) Catalysts Using Operando and Transient Spectroscopies. *Catal. Sci. Technol.* **2023**, *13*, 2922–2926.
28. Li, M.; Pham, T.H.M.; Oveisi, E.; et al. Revealing the Surface Chemistry for CO_2 Hydrogenation on Cu/CeO_{2-x} Using Near-Ambient-Pressure X-ray Photoelectron Spectroscopy. *ACS Appl. Energy Mater.* **2021**, *4*, 12326–12335.
29. Rabee, A.I.M.; Abed, H.; Vuong, T.H.; et al. CeO_2-Supported Single-Atom Cu Catalysts Modified with Fe for RWGS Reaction: Deciphering the Role of Fe in the Reaction Mechanism by *in Situ*/Operando Spectroscopic Techniques. *ACS Catal.* **2024**, *14*, 10913–10927.
30. Li, Y.; Kottwitz, M.; Vincent, J.L.; et al. Dynamic Structure of Active Sites in Ceria-Supported Pt Catalysts for the Water Gas Shift Reaction. *Nat. Commun.* **2021**, *12*, 914.
31. Yu, J.; Qin, X.; Yang, Y.; et al. Highly Stable Pt/CeO_2 Catalyst with Embedding Structure toward Water-Gas Shift Reaction. *J. Am. Chem. Soc.* **2024**, *146*, 1071–1080.
32. Reina, T.R.; Gonzalez-Castaño, M.; Lopez-Flores, V.; et al. Au and Pt Remain Unoxidized on a CeO_2-Based Catalyst during the Water-Gas Shift Reaction. *J. Am. Chem. Soc.* **2022**, *144*, 446–453.
33. Li, X.; Wang, X.; Beck, A.; et al. Quantifying Electronic and Geometric Effects on the Activity of Platinum Catalysts for Water-Gas Shift. *Nat. Commun.* **2025**, *16*, 6641.
34. Simanenko, A.; Kastenmeier, M.; Piliai, L.; et al. Probing the Redox Capacity of Pt–CeO_2 Model Catalysts for Low-Temperature CO Oxidation. *J. Mater. Chem. A* **2023**, *11*, 16659–16670.
35. Nie, L.; Mei, D.; Xiong, H.; et al. Activation of Surface Lattice Oxygen in Single-Atom Pt/CeO_2 for Low-Temperature CO Oxidation. *Science* **2017**, *358*, 1419–1423.
36. Caudillo-Flores, U.; Barba-Nieto, I.; Muñoz-Batista, M.J.; et al. Thermo-photo Production of Hydrogen Using Ternary Pt–CeO_2–TiO_2 Catalysts: A Spectroscopic and Mechanistic Study. *Chem. Eng. J.* **2021**, *425*, 130641.
37. Tavasoli, A.; Gouda, A.; Zähringer, T.; et al. Enhanced Hybrid Photocatalytic Dry Reforming Using a Phosphated Ni–CeO_2 Nanorod Heterostructure. *Nat. Commun.* **2023**, *14*, 1435.
38. Lorber, K.; Shvalya, V.; Zavašnik, J.; et al. Non-oxidative Calcination Enhances the Methane Dry Reforming Performance of Ni–CeO_{2-x} Catalysts under Thermal and Photo-thermal Conditions. *J. Mater. Chem. A* **2024**, *12*, 19910–19923.
39. Han, X.; Zhang, Z.; Dong, Y.; et al. Photothermal CO_2 Hydrogenation to CO on CeO_2 Catalyst via Redox Mechanism. *Chem. Eng. J.* **2025**, *510*, 161609.
40. Chu, S.; Yan, X.; Choi, C.; et al. Stabilization of Cu^+ by Tuning a CuO–CeO_2 Interface for Selective Electrochemical CO_2 Reduction to Ethylene. *Green Chem.* **2020**, *22*, 6540–6546.
41. Yan, X.; Chen, C.; Wu, Y.; et al. Efficient Electroreduction of CO_2 to C_2^+ Products on CeO_2 Modified CuO. *Chem. Sci.* **2021**, *12*, 6638–6645.
42. Patra, K.K.; Liu, Z.; Lee, H.; et al. Boosting Electrochemical CO_2 Reduction to Methane via Tuning Oxygen Vacancy Concentration and Surface Termination on a Copper/Ceria Catalyst. *ACS Catal.* **2022**, *12*, 10973–10983.
43. Xue, L.; Zhang, C.; Wu, J.; et al. Unveiling the Reaction Pathway on Cu/CeO_2 Catalyst for Electrocatalytic CO_2 Reduction to CH_4. *Appl. Catal. B Environ.* **2022**, *304*, 120951.
44. Jiang, Y.; Mao, K.; Li, J.; et al. Pushing the Performance Limit of Cu/CeO_2 Catalyst in CO_2 Electroreduction: A Cluster Model Study for Loading Single Atoms. *ACS Nano* **2023**, *17*, 2620–2628.
45. Kim, J.-H.; Shin, K.; Kawashima, K.; et al. Enhanced Activity Promoted by CeO_x on a CoO_x Electrocatalyst for the Oxygen Evolution Reaction. *ACS Catal.* **2018**, *8*, 4257–4265.
46. Huang, J.; Sheng, H.; Ross, R.D.; et al. Modifying Redox Properties and Local Bonding of Co_3O_4 by CeO_2 Enhances Oxygen Evolution Catalysis in Acid. *Nat. Commun.* **2021**, *12*, 3036.
47. Huang, J.; Hales, N.; Clark, A.H.; et al. Operando Tracking the Interactions between CoO_x and CeO_2 during Oxygen Evolution Reaction. *Adv. Energy Mater.* **2024**, *14*, 2303529.
48. Wang, Y.; Wang, S.; Wang, X.; et al. RuO_2–CeO_2 Lattice Matching Strategy Enables Highly Active and Stable Acidic Oxygen Evolution Electrocatalysis. *ACS Catal.* **2024**, *14*, 3298–3307.
49. Trovarelli, A.; Llorca, J. Ceria Catalysts at Nanoscale: How Do Crystal Shapes Shape Catalysis? *ACS Catal.* **2017**, *7*, 4716–4735.

50. Hu, Z.; Liu, X.; Meng, D.; et al. Effect of Ceria Crystal Plane on the Physicochemical and Catalytic Properties of Pd/Ceria for CO and Propane Oxidation. *ACS Catal.* **2016**, *6*, 2265–2279.
51. Rui, N.; Zhang, X.; Zhang, F.; et al. Highly Active Ni/CeO_2 Catalyst for CO_2 Methanation: Preparation and Characterization. *Appl. Catal. B Environ.* **2021**, *282*, 119581.
52. Hongmanorom, P.; Ashok, J.; Chirawatkul, P.; et al. Interfacial Synergistic Catalysis over Ni Nanoparticles Encapsulated in Mesoporous Ceria for CO_2 Methanation. *Appl. Catal. B Environ.* **2021**, *297*, 120454.
53. Sun, C.; Beaunier, P.; La Parola, V.; et al. Ni/CeO_2 Nanoparticles Promoted by Yttrium Doping as Catalysts for CO_2 Methanation. *ACS Appl. Nano Mater.* **2020**, *3*, 12355–12368.
54. Zhang, Z.; Yu, Z.; Feng, K.; et al. Eu^{3+}-Doping Promoted Ni–CeO_2 Interaction for Efficient Low-Temperature CO_2 Methanation. *Appl. Catal. B Environ.* **2022**, *317*, 121800.
55. Chen, S.; Costley-Wood, L.; Lezcano-Gonzalez, I.; et al. Understanding Defect Generation on CeO_2 and Its Utilization for Enhanced Metal‑Support Interactions in Ni/CeO_2 Catalysts for Improved CO_2 Methanation Performance. *Appl. Catal. B Environ. Energy* **2025**, *366*, 125029.
56. Lin, L.; Gerlak, C.A.; Liu, C.; et al. Effect of Ni Particle Size on the Production of Renewable Methane from CO_2 over Ni/CeO_2 Catalyst. *J. Energy Chem.* **2021**, *61*, 602–611.
57. Hao, Z.; Shen, J.; Lin, S.; et al. Decoupling the Effect of Ni Particle Size and Surface Oxygen Deficiencies in CO_2 Methanation over Ceria Supported Ni. *Appl. Catal. B Environ.* **2021**, *286*, 119922.
58. Adhikari, D.; Whitcomb, C.A.; Zhang, W.; et al. Revisiting the Influence of Ni Particle Size on the Hydrogenation of CO_2 to CH_4 over Ni/CeO_2. *J. Catal.* **2024**, *438*, 115708.
59. Chen, S.; Higgins, L.; Giarnieri, I.; et al. A Detailed Characterization Study of Ni/CeO_2 Catalysts Identifies Ni Availability as the Primary Factor Affecting CO_2 Methanation Performance. *J. Catal.* **2024**, *439*, 115778.
60. Martin, N.M.; Hemmingsson, F.; Schaefer, A.; et al. Structure–Function Relationship for CO_2 Methanation over Ceria Supported Rh and Ni Catalysts under Atmospheric Pressure Conditions. *Catal. Sci. Technol.* **2019**, *9*, 1644–1653.
61. Wang, F.; He, S.; Chen, H.; et al. Active Site Dependent Reaction Mechanism over Ru/CeO_2 Catalyst toward CO_2 Methanation. *J. Am. Chem. Soc.* **2016**, *138*, 6298–6305.
62. Guo, Y.; Mei, S.; Yuan, K.; et al. Low-Temperature CO_2 Methanation over CeO_2-Supported Ru Single Atoms, Nanoclusters, and Nanoparticles Competitively Tuned by Strong Metal–Support Interactions and H-Spillover Effect. *ACS Catal.* **2018**, *8*, 6203–6215.
63. Xu, X.; Liu, L.; Tong, Y.; et al. Facile Cr^{3+}-Doping Strategy Dramatically Promoting Ru/CeO_2 for Low-Temperature CO_2 Methanation: Unraveling the Roles of Surface Oxygen Vacancies and Hydroxyl Groups. *ACS Catal.* **2021**, *11*, 5762–5775.
64. Barba-Nieto, I.; Fernández-García, M.; Moncada, J.; et al. Activity and Selectivity for CO_2 Methanation of Clusters and Nanoplates of Ruthenium Dispersed on Ceria: In-situ Studies with XAFS and DRIFTS. *Catal. Today* **2025**, *459*, 115443.
65. Hemmingsson, F.; Schaefer, A.; Skoglundh, M.; et al. CO_2 Methanation over Rh/CeO_2 Studied with Infrared Modulation Excitation Spectroscopy and Phase Sensitive Detection. *Catalysts* **2020**, *10*, 601.
66. Yu, Z.-K.; Jiang, M.; Dai, S.; et al. Valence Restrictive Metal–Support Interaction for Boosting Catalytic Activity of Rh/CeO_2 in CO_2 Hydrogenation. *Nat. Commun.* **2025**, *16*, 9072.
67. Deng, K.; Lin, L.; Rui, N.; et al. Studies of CO_2 Hydrogenation over Cobalt/Ceria Catalysts with *in situ* Characterization: The Effect of Cobalt Loading and Metal–Support Interactions on the Catalytic Activity. *Catal. Sci. Technol.* **2020**, *10*, 6468–6482.
68. Evtushkova, A.; Heinrichs, J.M.J.J.; Parastaev, A.; et al. Flame Synthesized Co–CeO_2 Catalysts for CO_2 Methanation. *ACS Catal.* **2025**, *15*, 11217–11231.
69. Gao, Y.; Muravev, V.; Fan, Y.; et al. Strong Stabilization of Co Nanoparticles by CeO_{2-x} Clusters in Inverse CeO_x/Co Catalysts for Enhanced CO_2 Methanation. *Adv. Mater.* **2026**, *38*, e10593.
70. Deng, K.; Wang, Y.; Pérez-Bailac, P.; et al. Visualizing Size-Dependent Dynamics of $CeO_{2-\delta}${100}-Supported CoO_x Nanoparticles under CO_2 Hydrogenation Conditions. *J. Am. Chem. Soc.* **2025**, *147*, 19239–19252.
71. Yan, Y.; Wong, R.J.; Ma, Z.; et al. CO_2 Hydrogenation to Methanol on Tungsten-Doped Cu/CeO_2 Catalysts. *Appl. Catal. B Environ.* **2022**, *306*, 121098.
72. Kanuri, S.; Singh, S.A.; Uttaravalli, A.N.; et al. Morphologically Tuned CuO–ZnO–CeO_2 Catalyst for CO_2 Hydrogenation to Methanol. *RSC Adv.* **2024**, *14*, 10024–10033.
73. Almousawi, M.; Xie, S.; Kim, D.; et al. Hydroxyls on CeO_2 Support Promoting CuO/CeO_2 Catalyst for Efficient CO Oxidation and NO Reduction by CO. *Environ. Sci. Technol.* **2024**, *58*, 883–894.
74. Ziemba, M.; Weyel, J.; Hess, C. Elucidating the Mechanism of the Reverse Water-Gas Shift Reaction over Au/CeO_2 Catalysts Using Operando and Transient Spectroscopies. *Appl. Catal. B Environ.* **2022**, *301*, 120825.
75. Bansmann, J.; Abdel-Mageed, A.M.; Chen, S.; et al. Chemical and Electronic Changes of the CeO_2 Support during CO Oxidation on Au/CeO_2 Catalysts: Time-Resolved Operando XAS at the Ce LIII Edge. *Catalysts* **2019**, *9*, 785.
76. Bezkrovnyi, O.; Bruix, A.; Blaumeiser, D.; et al. Metal–Support Interaction and Charge Distribution in Ceria-Supported Au Particles Exposed to CO. *Chem. Mater.* **2022**, *34*, 7916–7936.

77. Piliai, L.; Matvija, P.; Dinhová, T.N.; et al. *In Situ* Spectroscopy and Microscopy Insights into the CO Oxidation Mechanism on Au/CeO_2(111). *ACS Appl. Mater. Interfaces* **2022**, *14*, 56280–56289.
78. Soler, L.; Casanovas, A.; Escudero, C.; et al. Ambient Pressure Photoemission Spectroscopy Reveals the Mechanism of Carbon Soot Oxidation in Ceria-Based Catalysts. *ChemCatChem* **2016**, *8*, 2748–2751.
79. Toscani, L.M.; Zimicz, M.G.; Martins, T.S.; et al. *In situ* X-ray Absorption Spectroscopy Study of CuO–NiO/CeO_2–ZrO_2 Oxides: Redox Characterization and Its Effect in Catalytic Performance for Partial Oxidation of Methane. *RSC Adv.* **2018**, *8*, 12190–12202.
80. Hoque, K.A.; Sathi, S.A.; Akter, F.; et al. Recent Advances on Photocatalytic CO_2 Reduction Using CeO_2-Based Photocatalysts: A Review. *J. Environ. Chem. Eng.* **2024**, *12*, 113487.
81. Zhu, H.; Fu, X.; Zhou, Z. 3D/2D Heterojunction of CeO_2/Ultrathin MXene Nanosheets for Photocatalytic Hydrogen Production. *ACS Omega* **2022**, *7*, 21684–21693.
82. Mansingh, S.; Kandi, D.; Das, K.K.; et al. A Mechanistic Approach on Oxygen Vacancy-Engineered CeO_2 Nanosheets Concocts over an Oyster Shell Manifesting Robust Photocatalytic Activity toward Water Oxidation. *ACS Omega* **2020**, *5*, 9789–9805.
83. Zheng, J.; Li, S.; Zhang, Y.; et al. Ag–O–Ce^{3+} Atomic Interface and Surface Oxygen Vacancies on CeO_2 Synergistically Promoted the Selective Visible Photocatalytic Reduction of Carbon Dioxide. *J. Mater. Chem. C* **2023**, *11*, 7320–7330.
84. Ren, Y.; Fu, Y.; Li, N.; et al. Concentrated Solar CO_2 Reduction in H_2O Vapour with >1% Energy Conversion Efficiency. *Nat. Commun.* **2024**, *15*, 4675.
85. Sun, J.; Bai, Y.; Feng, X.; et al. Zn_2GeO_4@CeO_2 Core@Shell Nanorods for Efficient Photocatalytic CO_2 Reduction. *Molecules* **2025**, *30*, 2205.
86. Yang, S.; Zhang, W.; Pan, G.; et al. Photocatalytic Co-Reduction of N_2 and CO_2 with CeO_2 Catalyst for Urea Synthesis. *Angew. Chem. Int. Ed.* **2023**, *62*, e202312076.
87. Zhang, K.; Xu, C.; Zhang, X.; et al. Structural Heredity in Catalysis: CO_2 Self-Selective CeO_2 Nanocrystals for Efficient Photothermal CO_2 Hydrogenation to Methane. *Small* **2024**, *20*, 2308823.
88. Liang, Y.; Wu, C.; Meng, S.; et al. Ag Single Atoms Anchored on CeO_2 with Interfacial Oxygen Vacancies for Efficient CO_2 Electroreduction. *ACS Appl. Mater. Interfaces* **2023**, *15*, 30262–30271.
89. Yu, R.; Qiu, C.; Lin, Z.; et al. CeO_x Promoted Electrocatalytic CO_2 Reduction to Formate by Assisting in the Critical Hydrogenation Step. *ACS Mater. Lett.* **2022**, *4*, 1749–1755.
90. Liu, H.; Li, B.; Liu, Z.; et al. Ceria-Mediated Dynamic Sn^0/$Sn^{\delta+}$ Redox Cycle for CO_2 Electroreduction. *ACS Catal.* **2023**, *13*, 5033–5042.
91. Yao, N.; Meng, R.; Wu, F.; et al. O_{vs}-Induced CeO_2/Co_4N Heterostructures toward Enhanced pH-Universal Hydrogen Evolution Reactions. *Appl. Catal. B Environ.* **2020**, *277*, 119282.
92. Zhou, P.; Hai, G.; Zhao, G.; et al. CeO_2 as an Electron Pump to Boost the Performance of Co_4N in Electrocatalytic Hydrogen Evolution, Oxygen Evolution and Biomass Oxidation Valorization. *Appl. Catal. B Environ.* **2023**, *325*, 122364.
93. Zhao, G.; Hai, G.; Zhou, P.; et al. Electrochemical Oxidation of 5-Hydroxymethylfurfural on CeO_2-Modified Co_3O_4 with Regulated Intermediate Adsorption and Promoted Charge Transfer. *Adv. Funct. Mater.* **2023**, *33*, 2213170.
94. Sanghez de Luna, G.; Zeller, P.; Öztuna, E.; et al. *In Situ* Development of a 3D Cu–CeO_2 Catalyst Selective in the Electrocatalytic Hydrogenation of Biomass Furanic Compounds. *ACS Catal.* **2023**, *13*, 12737–12745.